Title

3D-Printed Graded Electrode with Ultrahigh MnO2 Loading for Non-Aqueous Electrochemical Energy Storage

Journal

Advanced Energy Materials, 13(20)

ISSN

1614-6832

Authors

Lin, Dun

Chandrasekaran, Swetha

Forien, Jean-Baptiste

et al.

Publication Date

2023-05-01

DOI

10.1002/aenm.202300408

WILEY-VCH

3D-printed Graded Electrode with Ultrahigh MnO_2 Loading for Non-aqueous Electrochemical Energy Storage

Dun Lin, Swetha Chandrasekaran, Jean-Baptiste Forien, Xinzhe Xue, Anica Pinongcos, Emma Coester, Marcus A. Worsley, and Yat Li**

D. Lin, X. Xue, A. Pinongcos, E. Coester and Prof. Y. Li

Department of Chemistry and Biochemistry

University of California

1156 High Street, Santa Cruz, CA 95064, United States

Dr. S. Chandrasekaran, Dr. J.-B. Forien and Dr. M. A. Worsley

Lawrence Livermore National Laboratory

7000 East Avenue, Livermore, CA 94550, United States

Keywords: Additive manufacturing, manganese dioxide, graded lattice structure, non-aqueous electrolyte, electrochemical energy storage

Abstract

Electrolytic manganese dioxide (MnO_2) is one of the promising cathode candidates for electrochemical energy storage devices due to its high redox capacity and ease of synthesis. Yet, high-loading MnO_2 often suffers from sluggish reaction kinetics, especially in non-aqueous electrolytes. The non-uniform deposition of MnO_2 on porous current collector also makes it difficult to fully utilize the active materials at high mass loading. Here, we develop a 3D printed graded graphene aerogel (3D GA) that contains sparsely separated exterior ligaments to create large open channels for mass transport as well as densely arranged interior ligaments providing large ion accessible active surface. The unique structural design homogenized the thickness of electrodeposited MnO_2 even at an ultrahigh mass loading of ~ 70 mg cm^{-2}. The electrode achieves a remarkable volumetric capacity of 29.1 mA h cm^{-3} in the non-aqueous electrolyte. A Li-ion hybrid capacitor device assembled with graded 3D GA/MnO_2 cathode and graded 3D GA/VO_x anode exhibits a wide voltage window of 0~4 V and a superior volumetric energy density of 20.2 W h L^{-1}. The findings offer guidance on 3D printed electrode design for supporting ultrahigh loading of active materials and developments of high energy density energy storage devices.

The capability to deliver plenty of electrical energy within a compact device configuration is one of the major pursuits of many electrochemical energy storage devices, such as portable batteries, on-chip micro-supercapacitors, and power supplies of electric vehicles, *etc*.[1] Such capability can be quantified by volumetric energy density, which is determined by the volumetric capacity (charge delivered per volume) and the output voltage of the device according to the following equation:

$$E_{\mathrm{V}} = \frac{\int_0^q U(q)dq}{V} = \frac{\int_0^U q(U)dU}{V} \quad (1)$$

Where E_{V} is the volumetric energy density (mW h cm^{-3} or W h L^{-1}), q is the device output charge (mA h), U is the device output voltage, and V is the device volume (cm^3).[1f, 2] Electrodes featuring high volumetric capacities and high cathodic/low anodic operating potentials are keys to achieving outstanding volumetric energy density at the device level.[1f, 3]

Among numerous candidate electrode materials, electrolytic manganese dioxide (MnO_2) has been frequently reported as a cathode that can achieve ultrahigh areal mass loading through facile electrodeposition techniques and deliver high volumetric capacity for aqueous supercapacitors and batteries.[4] Yet, to increase device output voltage, stable non-aqueous electrolytes are more preferrable than aqueous electrolytes, which typically limit the output voltages to less than 2 V because of the water splitting reaction.[5] Therefore, the coupling of ultrahigh-loading electrolytic MnO_2 cathodes and non-aqueous electrolytes is logical and promising for achieving high volumetric energy density. Unfortunately, the electrochemical performance of MnO_2 decreases rapidly with increase of mass loading (i.e. thick MnO_2 layers) because of its intrinsically low electrical conductivity, sluggish ion diffusion and conduction in non-aqueous electrolyte, and slow kinetics of the dominant aprotic redox reactions (*e.g.*, Li^+ ion insertion/desertion).[6]

Recently, the concept of conductive 3D-printed lattice current collectors has been proven to enable efficient electron transport and ion diffusion of ultrahigh-loading of MnO_2 for

energy-dense aqueous supercapacitors.[4a, 4b] A 3D-printed graphene aerogel (3D GA) scaffold with orthogonal lattice structure and ordered large channels was able to support MnO_2 at an unprecedented loading level of hundreds mg cm^{-2}, while maintaining high gravimetric capacitance, volumetric capacitance and rate capability at electrode thicknesses up to few millimeters.[4a] This excellent performance was attributed to the good electrical conductivity of the interconnected network of the 3D GA, and efficient ion transport benefiting from the low-tortuosity porous architecture. This strategy simultaneously enhances the accessibility of ultrahigh-loading MnO_2 to electrons and electrolyte ions compared to the conventional planar MnO_2 electrodes. Here, we extend this concept to non-aqueous energy storage systems by further optimizing the electrode architecture to improve the uniformity of MnO_2 deposition and to promote the MnO_2 accessibility during charge/discharge.

We develop a modified 3D GA substrate with graded porous structure (**Figure 1**). The center-to-center ligament spacing of the graded structure gradually decreases from the outer layer to the inner layer, in contrast to the conventional non-graded lattice that has a fixed center-to-center ligament spacing. The gradient porous design facilitates ion/electrolyte diffusion throughout the entire GA for achieving uniform electrodeposition of MnO_2. At ultrahigh MnO_2 loadings (up to ~70 mg cm^{-2}), the 3 mm thick graded 3D GA/MnO_2 composite electrode delivers an excellent volumetric capacity of 29.1 mA h cm^{-3} at a high current density of 20 mA cm^{-2} in the non-aqueous electrolyte, outperforming other previously reported 3D printed and/or high-MnO_2-loaded thick cathodes. The graded scaffold also considerably improves the high-rate capacity retention compared to the non-graded counterpart, due to uniform deposition of MnO_2 in 3D structure and enhanced MnO_2 accessibility. A non-aqueous lithium-ion hybrid capacitor fabricated by a 3D graded MnO_2 cathode and a 3D graded VO_x anode achieves a wide voltage window of 4 V and an excellent volumetric energy density of 20.2 W h L^{-1}. The structural optimization offers new opportunities for homogenizing the thickness of

electrodeposited high-loadings of active materials on thick and porous substrates as well as improving the rate performance of high-energy-density electrochemical energy storage systems.

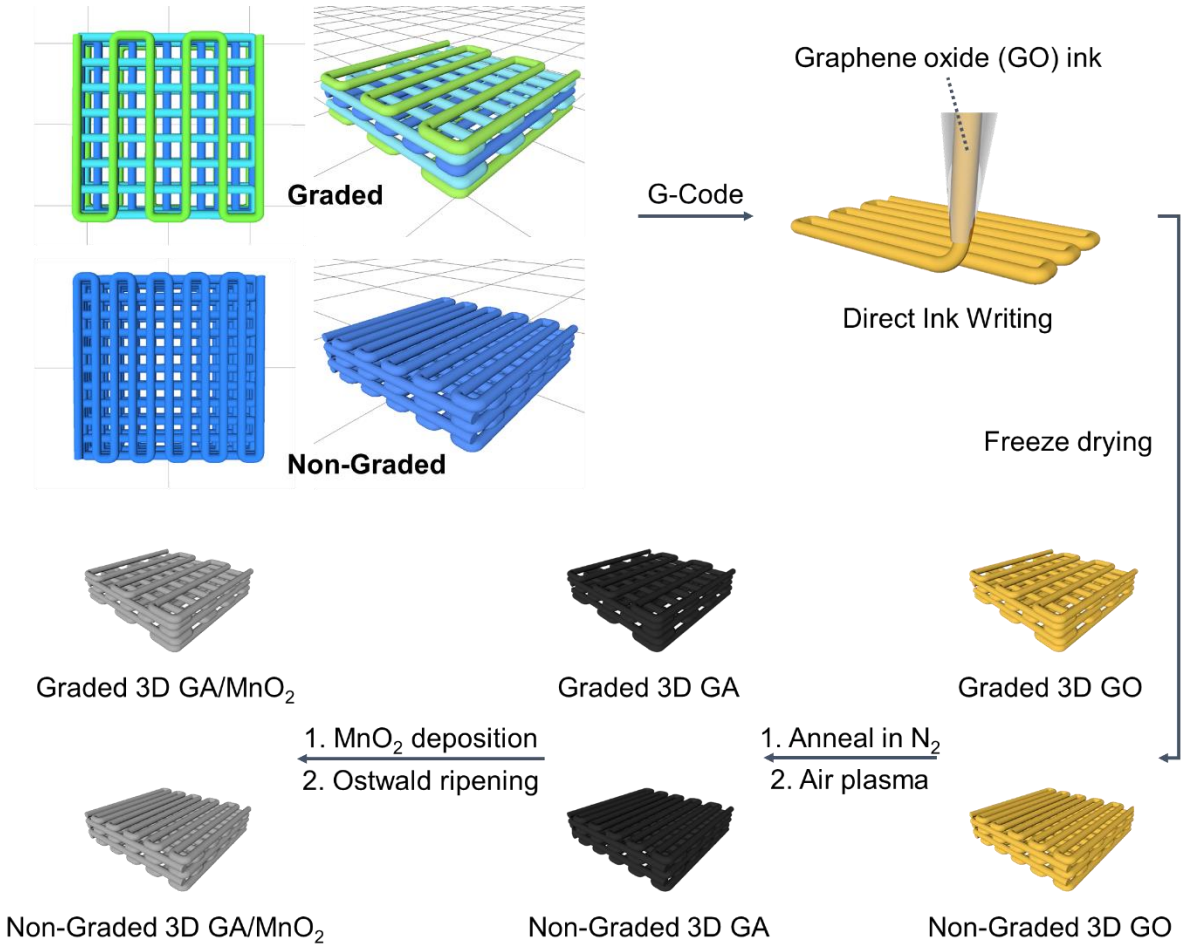

Figure 1. Schematic illustration of the fabrication process of non-graded and graded 3D GA/MnO_2 composite electrodes.

Figure 1 illustrates the fabrication process of the non-graded and graded 3D GA/MnO_2. The conventional non-graded structure was constructed by a simple cubic lattice with multiple orthogonal layers of parallel cylindrical rod ligaments.[4a, 4b] The diameter of the cylindrical rods is set to 200 µm and the center-to-center rod spacing is 0.4 mm for each of the total 18 layers. Therefore, the size of the open channels is constantly 200 µm x 200 µm throughout the entire z-direction. The layer projections overlap with each other. For the graded simple cubic lattice, the orthogonal layers are also composed of parallel cylindrical rods with a diameter of 200 µm,

while the layer spacing of every 2 layers gradually decreases to a minimum and then gradually increases from bottom to top. Specifically, the first 2 layers have a center-to-center rod spacing of 1.2 mm, followed by 1.0 mm spacing (layers 3&4), 0.8 mm (layers 5&6), 0.6 mm (layers 7&8), and 0.4 mm (layers 9&10). Subsequently, the spacing gradually increases from 0.4 mm to 1.2 mm every 2 layers till the top. Such a graded structure was designed with the intention that the open channels at the exterior domains (top and bottom surface layers) would allow for maximum ion flux, while the densely placed cylindrical rods at the interior domains (center layers) would provide an enlarged available surface for electrochemical processes. Moreover, we anticipated that the cylindrical rods in the interior of the graded structure would be more exposed than those of the non-graded structure due to the reduced overlap of layer projections. After generating G-codes from the models, the 3D structures were printed using the direct ink writing technique, where the aqueous ink contained single-layer graphene oxide (GO) sheets suspension (40 mg/mL) mixed with 5% hydroxypropyl methylcellulose and was extruded through a 200 μm nozzle. The 3D printed GO structures were first freeze dried and then annealed in nitrogen atmosphere at 1050 °C to convert GO to graphene. The samples were further air plasma treated for better wettability and MnO_2 affinity. The resultant 3D GA samples have a reasonably low mass density of ~33 mg cm^{-3}. As shown in Figure S1 (Supporting Information), the parallel cylindrical rods composing each orthogonal layer of the printed lattice structure have a diameter of 200 μm, a porous morphology of interconnected graphene sheets, and a gradual variation of the center-to-center rod spacing, as designed. The surface of rods even in the inner layers are visible from the top view, ensuring a higher accessibility for electrolyte and ions. On the contrary, the cylindric rods on each layer of non-graded 3D GA were stacked together with a fixed center-to-center spacing of 0.4 mm, forming narrow open channels and overshadowing the rods beneath (Figure S2, Supporting Information).

Subsequently, MnO_2 nanosheets were pulse-electrodeposited onto the 3D GA substrates followed by an Ostwald ripening treatment to obtain the composite electrode (3D GA/MnO_2).

The Ostwald ripening treatment was reported to be useful in improving the MnO_2 electrical conductivity and facilitates the ion transfer in MnO_2.[4c] The MnO_2 mass loadings obtained at different numbers of pulse electrodeposition cycles are depicted in Table S1 (Supporting Information). After 60 pulse cycles, the obtained graded 3D GA/MnO_2-60 reached a high MnO_2 mass loading of 22.7 mg cm^{-2}. Significantly, the deposited MnO_2 nanosheets are conformally coated on the cylindric rods including the interior layers, inheriting the porous morphology of the underlying 3D GA substrate (**Figure 2a** and Figure S3, Supporting Information). X-ray diffraction (XRD) and X-ray photoelectron spectroscopy (XPS) results confirmed the nanosheets are ε-MnO_2 (Figures S4 and S5, Supporting Information).[4a, 4c] The MnO_2 mass loading also increases linearly with the number of pulse electrodeposition cycles. The graded electrodes prepared by 120 (3D GA/MnO_2-120) and 180 (3D GA/MnO_2-180) cycles achieve ultrahigh MnO_2 loadings of 47.3 mg cm^{-2} and 67.7 mg cm^{-2}, respectively. As shown in **Figures 2b and 2c**, these samples also maintain a conformal MnO_2 coating. Notably, the thickening of MnO_2 layers does not block the open channels, retaining good accessibility to the interior of 3D GA scaffold. In contrast, the non-graded 3D GA/MnO_2 samples suffered from severe shrinkage of open channels due to excess coating of MnO_2 on the scaffold's exterior surface (Figure S6, Supporting Information). Non-destructive micro computed tomography (micro-CT) was employed to visualize the distributions of MnO_2 deposits on the ligaments along the z-direction (**Figures 2d-f** and Figure S7, Supporting Information). The bright contrast region represents the MnO_2 coating on scaffold surface. The coating thickness increases with the number of pulse electrodeposition cycles (mass loading) for both non-graded and graded samples. For graded 3D GA/MnO_2 samples, uniform MnO_2 coatings can be clearly observed even on the surface of middle layers (**Figures 2d-f**), suggesting the surface of these interior ligaments are readily accessible by Mn^{2+} ions during electrodeposition. On the contrary, the MnO_2 signal is relatively weak in the interior domains of the non-graded 3D GA/MnO_2 (Figure S7, Supporting Information) and indicated that most MnO_2 was deposited on the exterior

surface of the GA substrate (edges of the cross-section image). These results confirm the critical role of open channels of the graded structure in improving the uniformity of deposited MnO_2 by allowing efficient transport of ions into the interior part of 3D GA substrate during electrodeposition. In the meantime, the densely packed interior structure guarantees large electrochemically active surface area for supporting high loading of MnO_2.

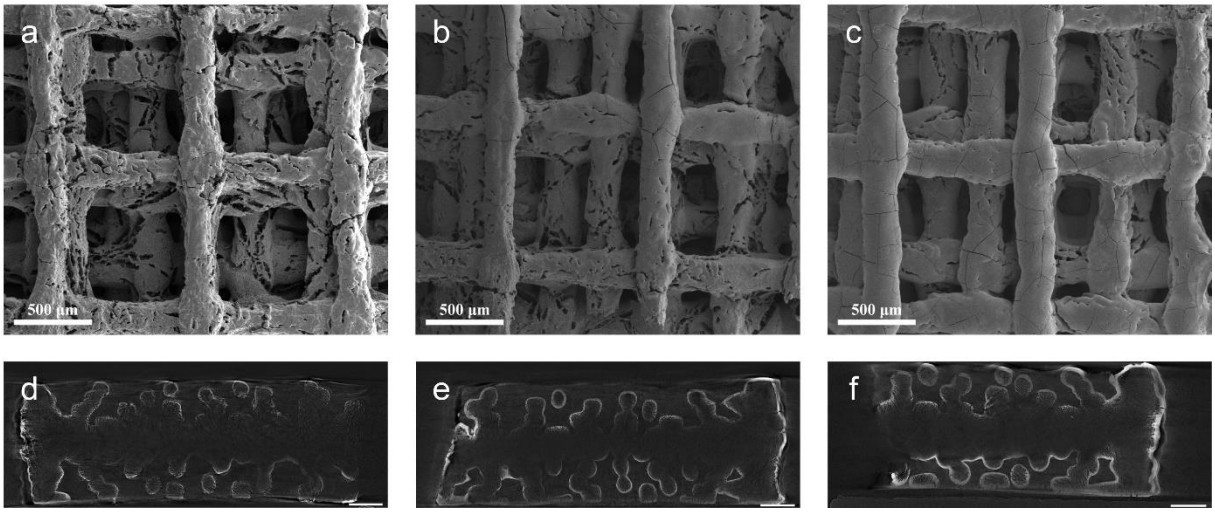

Figure 2. Top-view SEM images of (a) graded 3D GA/MnO_2-60 (22.7 mg cm^{-2}), (b) graded 3D GA/MnO_2-120 (47.3 mg cm^{-2}), and (c) graded 3D GA/MnO_2-180 (67.7 mg cm^{-2}). Side-view cross-section micro-CT images of (d) graded 3D GA/MnO_2-60, (e) graded 3D GA/MnO_2-120, and (f) graded 3D GA/MnO_2-180. Scale bars of CT images are 500 μm.

The electrochemical performance of both non-graded and graded 3D GA/MnO_2 with different MnO_2 loadings were evaluated in a non-aqueous 1 M $LiClO_4$/acetonitrile electrolyte using a three-electrode system under dry Ar atmosphere (Experimental Section). The galvanostatic charge/discharge (GCD) voltage profiles are illustrated in **Figure 3a**, Figures S8 and S9 (Supporting Information). In contrast to the limited voltage windows (typically 0.8~1.2 V) in aqueous electrolytes, the use of Li-ion-based non-aqueous electrolyte effectively expands the stable voltage window to 2.2 V (-0.8~1.4 V *vs.* Pt). Redox reactions can take place in this wide voltage window, such as:

$$MnO_2 + xLi^+ + xe^- \leftrightarrow Li_xMnO_2 \quad (2)$$

where *x* represents the number of moles of Li ions and electrons involved in the Li^+ intercalation (discharge) and de-intercalation (charge) reactions.[6a] The charge/discharge curves with nearly constant slopes indicate a capacitor-battery hybrid behavior. **Figure 3b** shows the volumetric capacities of graded 3D GA/MnO_2 with different MnO_2 loadings obtained at different rates. Benefiting from the high materials loading capability and improved ion transport provided by the 3D GA scaffold, the graded 3D GA/MnO_2 electrodes can operate at a range of ultrahigh areal current densities of 20~100 mA cm^{-2}, resulting in remarkable volumetric capacities up to 29.1 mA h cm^{-3} at the current density of 20 mA cm^{-2}. Note that the volumetric capacity increases with the mass loading, indicating the unimpeded ion transport even at high mass loadings and high rates. Importantly, despite the graded 3D GA having less surface area (less printed ligaments) per unit volume for MnO_2 electrodeposition, the maximum volumetric capacities at 20 mA cm^{-2} with different loadings are comparable to those of non-graded 3D GA/MnO_2 electrodes (Figure S10, Supporting Information). The obtained volumetric capacities are higher than the values reported for most 3D printed and/or high-MnO_2-loaded thick cathodes (**Figure 3c** and Table S2, Supporting Information).[4a, 4c, 7] It is noteworthy that these volumetric capacities were achieved at an outstanding current density (20 mA cm^{-2} or ~0.3 A g^{-1}), which is also among the highest in previous studies (Table S2, Supporting Information). Finally, the graded 3D GA/MnO_2-180 retained 86.4% of capacity after 1000 charge/discharge cycles at 100 mA cm^{-2} without noticeable morphological change (Figures S11 and S12, Supporting Information), reflecting its good potential for practical applications.

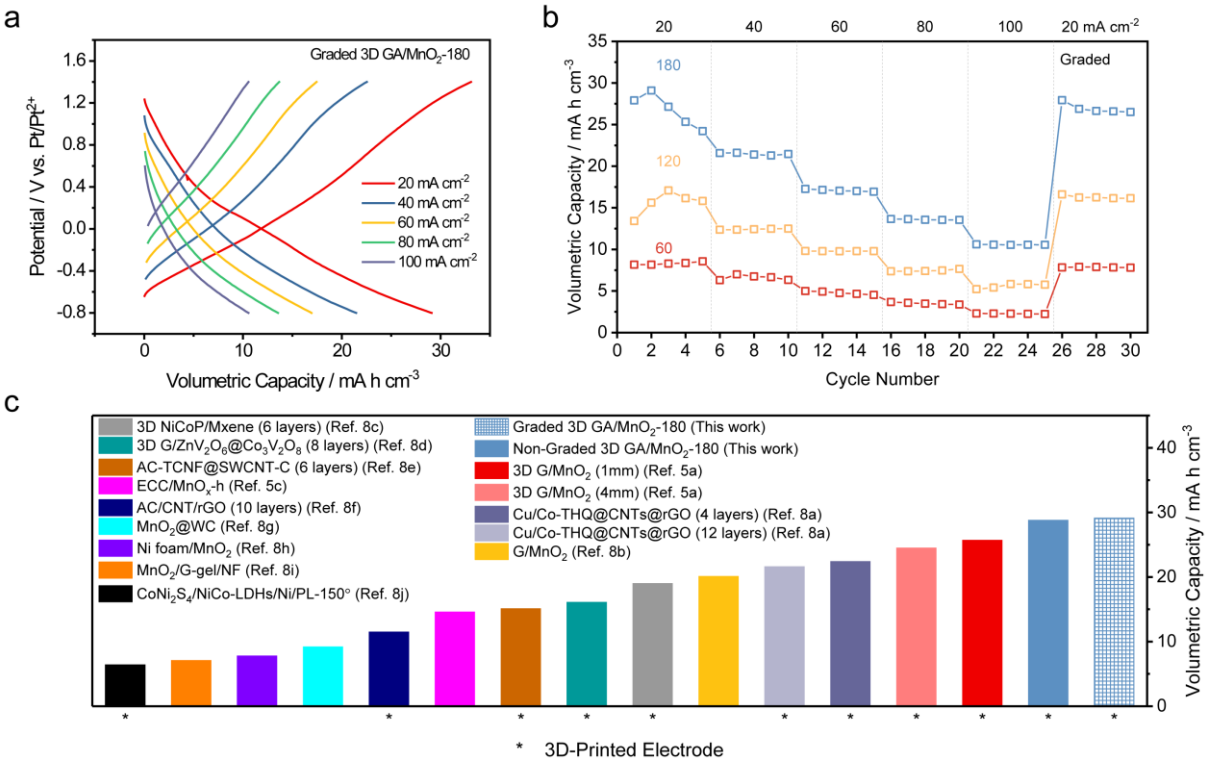

Figure 3. (a) GCD voltage profiles of graded 3D GA/MnO_2-180 (67.7 mg cm^{-2}). (b) Volumetric capacity retention of graded 3D GA/MnO_2 obtained at different current densities. (c) A plot compares the volumetric capacity of non-graded 3D GA/MnO_2-180 (68.7 mg cm^{-2}) and graded 3D GA/MnO_2-180 (67.7 mg cm^{-2}) with the values of previously reported for 3D printed and/or high-MnO_2-loaded thick cathodes.[4a, 4c, 7]

Despite the graded and non-graded electrodes having similar volumetric capacitance at 20 mA cm^{-2}, the graded electrode shows considerably better capacity retention. As shown in **Figure 4a**, compared to the non-graded electrode, the graded 3D GA/MnO_2-180 exhibits not only higher volumetric capacities but also better capacity retentions at measured current densities (39.5% vs. 29.0%) and the improved capacity retention implies faster kinetics exhibited by the system. We also performed electrochemical impedance spectroscopy and fitted the data with proper equivalent circuits to deconvolute resistances of different electrochemical processes, including series resistance (R_s), charge transfer resistance (R_{ct}), diffusion resistance (R_d), and diffusion time constant (τ_d) (**Figure 4b**). Noted that R_d and τ_d were obtained from the restricted

diffusion element *M*, which is used for diffusions involving Li^+ ion insertion/desertion. Both graded and non-graded 3D GA/MnO_2-180 have comparable series resistance and charge transfer resistance. The greatest difference observed between them is in diffusion resistance. The graded electrode has a diffusion resistance of 11.19 Ω and a diffusion time constant of 4.946 s, which are substantially smaller than that of the non-graded electrode (38.25 Ω and 11.12 s, respectively), representing a less impeded and more efficient ion diffusion process in the graded structure. Smaller diffusion resistance is critical for sufficient ion supply and thus preserving a high degree of active material utilization during fast charge/discharge.

To quantitatively unveil the portions of capacity originating from fast reversible surface electrochemical reactions, Trasatti capacity contribution analysis was performed.[4c, 8] The gravimetric capacities based on MnO_2 mass loadings are calculated from cyclic voltammetry curves (Figure S13, Supporting Information) and plotted against $v^{-1/2}$ (v is scan rate), as shown in **Figure 4c**. By assuming semi-infinite ion diffusion, a linear fitting line at low scan rates can be extrapolated to determine y-intercept ($v \rightarrow +\infty$) that represents the gravimetric capacity contributed by the surface ($Q_{surface}$). Compared to non-graded electrode, the graded 3D GA/MnO_2-180 prevailed not only in the total gravimetric capacity at all scan rates, but also in $Q_{surface}$ with a nearly one-fold increase from 22.7 to 46.9 mA h g^{-1}. At a low scan rate of 1 mV s^{-1}, $Q_{surface}$ of graded 3D GA/MnO_2-180 contributed 62.0% of the total capacity, while the non-graded counterpart is only 32.4% (**Figure 4d**). When the scan rate increased to 5 mV s^{-1}, the contribution from $Q_{surface}$ was further increased to 78.7% for graded 3D GA/MnO_2-180, while merely 53.0% for non-graded 3D GA/MnO_2-180. These results again support better accessibility and utilization of MnO_2 benefited by the graded structure, as the enlarged exterior pores guaranteed higher Li^+ ion flux to reach the interior domains (**Figure 4f**).

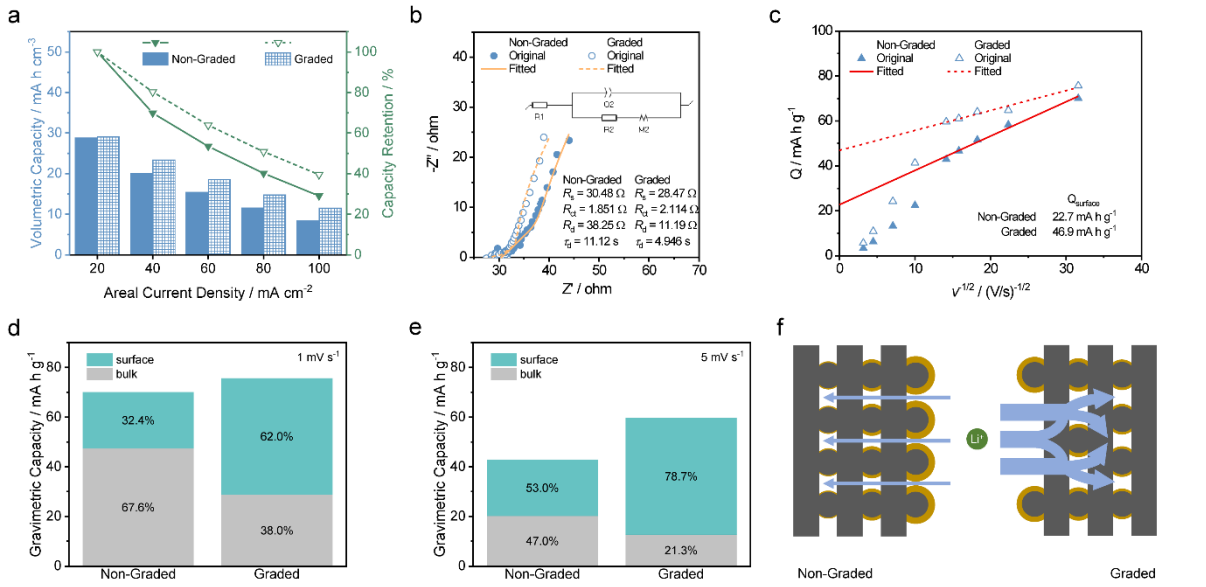

Figure 4. (a) Comparisons of volumetric capacities and capacity retentions at different areal current densities between non-graded 3D GA/MnO_2-180 (68.7 mg cm^{-2}) and graded 3D GA/MnO_2-180 (67.7 mg cm^{-2}); (b) Nyquist plots and the fitted results of non-graded and graded 3D GA/MnO_2-180; (c) Plot of gravimetric capacity (Q) vs. $v^{-1/2}$ for non-graded and graded 3D GA/MnO_2-180. Histogram illustrations of surface capacity contributions in non-graded and graded 3D GA/MnO_2-180 at a scan rate of (d) 1 mV s^{-1} and (e) 5 mV s^{-1}. (f) Schematic illustration of the Li^+ ion flux in graded *vs.* non-graded structure.

The graded 3D GA/MnO_2-180 (68.2 mg cm^{-2}) electrode was paired with a graded 3D GA anode electrodeposited with mixed-valence vanadium oxide (3D GA/VO_x, 33.3 mg cm^{-2}) to assemble a non-aqueous Li-ion hybrid capacitor device (Figure S14, Supporting Information). A high output voltage of 4 V was achieved (**Figure 5a**), accompanied with a typical capacitor-battery hybrid behavior within this wide voltage window (**Figure 5b**). Impressive maximum volumetric capacity of 11.6 mA h cm^{-3} (**Figure 5c**) and maximum volumetric capacitance of 11.9 F cm^{-3} (Figure S15, Supporting information) were achieved, ultimately leading to large volumetric energy density of 20.2 W h L^{-1} compared against other reported 3D-structured supercapacitors and Li-ion hybrid capacitors (**Figure 5d**), such as

G/ZnV_2O_6@$Co_3V_2O_8$//G/VN[7d], MnO_2@WC//AWC[7g], AC-TCNF@SWCNT-C symmetric supercapacitor (SSC)[7f], 3D G/MnO_2 SSC[4a], 3D GA/MnO_2//SF-3D GA[4b], 3D-GCA SSC[9], *etc*.

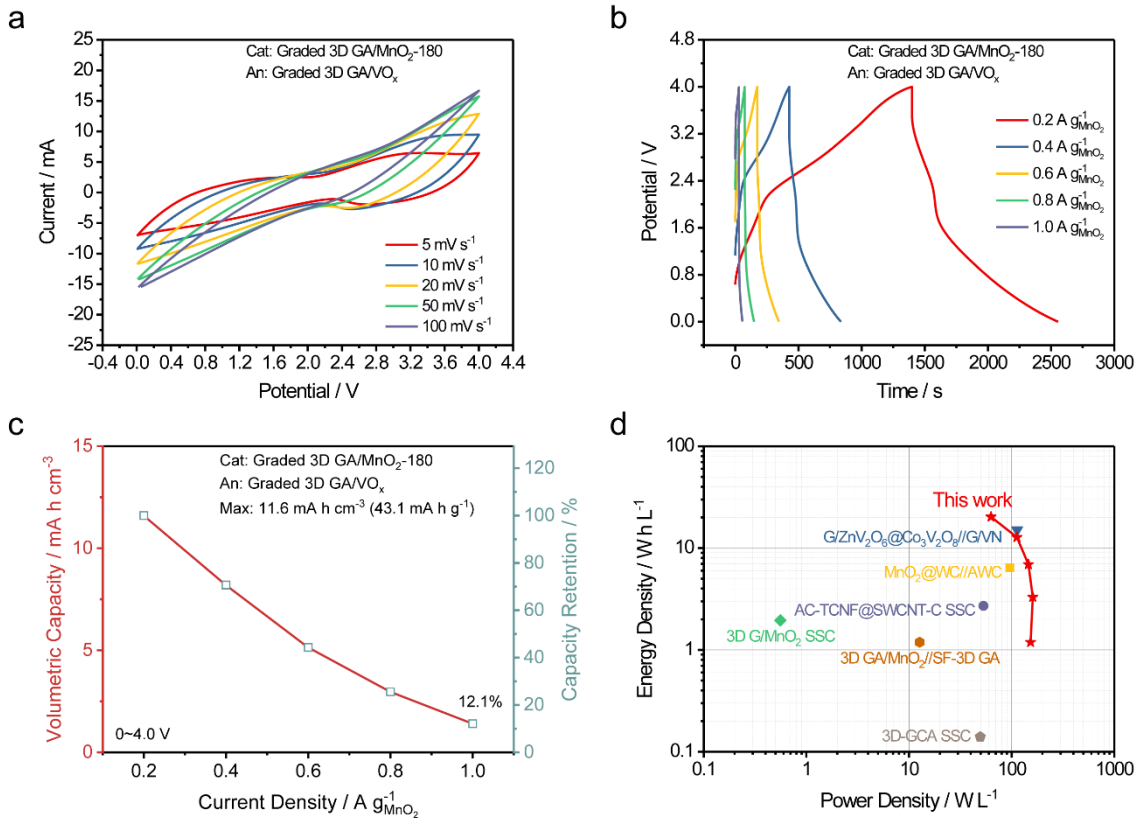

Figure 5. (a) Cyclic voltammetry curves, (b) galvanostatic charge/discharge curves, and (c) volumetric capacity and capacity retention of the graded 3D/GA-MnO_2-180//3D GA/VO_x Li-ion hybrid capacitor device. (d) Ragone plot of the graded 3D/GA-MnO_2-180//3D GA/VO_x device. Values reported for other 3D-structured supercapacitors and Li-ion hybrid capacitors are added for comparison.[4a, 4b, 7d, 7f, 7g, 9]

In conclusion, we have demonstrated a 3D printed graded structure that can better accommodate ultrahigh loading of MnO_2 than conventional lattice structure by homogenizing the MnO_2 film thickness and uniformity. The large exterior pores in the graded structure allow efficient ion diffusion during electrodeposition and charge/discharge cycling, while the densely arranged interior ligaments provide large ion-accessible active surface. The graded 3D GA/MnO_2-180

cathode achieves a record high maximum volumetric capacity of 29.1 mA h cm^{-3} at a high current density of 20 mA cm^{-2} with a wide voltage window of 2.2 V in the non-aqueous electrolyte, outperforming most reported 3D printed and/or high-MnO_2-loaded thick cathodes. Significantly, the electrodes show good capacity retention even at current densities as high as 100 mA cm^{-2}, which can be ascribed to the efficient ion transport into the interior domains of the electrode through the unimpeded open channels of the graded scaffold. The assembled Li-ion hybrid capacitor device with graded 3D GA/MnO_2-180 cathode and graded 3D GA/VO_x anode exhibits a wide voltage window of 0~4 V and a superior volumetric energy density of 20.2 W h L^{-1}. These findings can inspire future development of thick and porous substrates for electrodeposition of high-loading materials and improve capacitance retention and volumetric energy density.

Experimental Methods

Ink Preparation.

Single layer graphene oxide sheets (GO) having a lateral dimension of 300-800 nm purchased from Cheaptubes Inc. were used to prepare the aerogel inks. The GO suspension was prepared by ultra-sonicating 0.8 g of GO in 20 g of water for 24 h in a temperature-controlled sonication bath. This combination yields a GO concentration of 40 mg/ml. The suspension is then mixed with 5 wt.% of hydroxypropyl methylcellulose (from DOW chemicals) GO-ink in a planetary Thinky mixer at 2000 rpm until the cellulose was fully mixed without any agglomerates.

3D Printing of Graphene Oxide.

The ink was loaded into a 10 ml syringe barrel (EFD) and centrifuged for a minute at 4500 rpm to remove air bubbles, after which the ink is extruded through a micro nozzle (200 µm diameter) to pattern 3D structures on a glass substrate. For direct ink writing, the syringe was attached by a luer-lock to a smooth-flow tapered nozzle whose inner diameter(d) is 200

μm. The ink was then extruded by means of an air powered fluid dispenser (Ultimus V, EFD) which provides an appropriate pressure (in the range of 18-30 psi) for writing and the writing speed was kept at 10 mm/sec for all the 3D printed structures. Although it is not mandatory to change the PTFE nozzle tip between the prints, for the fabrication of electrodes, a new tip was used for every sample.

Two types of simple cubic lattices, namely non-graded and graded structures, were printed on a glass substrate by varying the spacing between the ligaments. For the non-graded sample, simple cubic lattice with multiple orthogonal layers of parallel cylindrical rods were printed alternately. The diameter of the cylindrical rods equals the diameter of nozzle and the center-to-center rod spacing of 0.4 mm (for 200 μm nozzle). The height of the electrodes was set at 2.16 mm (18 layers) and the layers were stacked on the structure such that each layer has a *z*-spacing of 0.12 mm. For the graded simple cubic lattice, multiple orthogonal layers of parallel cylindrical rods were printed alternately using a 200 μm nozzle with similar *z*-spacing but the layer spacing after every 2 layers gradually decreased to a minimum and then gradually increased as the structure was built. The first 2 layers had a center-to-center rod spacing of 1.2 mm, followed by 1.0 mm spacing (layers 3&4), 0.8 mm (layers 5&6), 0.6 mm (layers 7&8), 0.4 mm (layers 9&10). After which, the spacing gradually increased from 0.4 mm to 1.2 mm every 2 layers till the top. To avoid cracking or drying due to evaporation of water, soon after printing, the 3D printed structures were immersed in liquid nitrogen and freeze dried for 48 h in vacuum.

Synthesis of 3D Graphene Aerogel.

The 3D printed graphene oxide aerogels were subjected to a heat treatment process where the samples were first annealed in air at 240 °C and later pyrolyzed in a tube furnace under nitrogen atmosphere at 1000 °C for 1h with a heating rate of 0.5°C/min to form graphene aerogels. To further improve the wettability of the aerogels for electrodeposition, the samples

were treated in air plasma for 4 minutes using a Harrick basic plasma cleaner with adjustable RF power. The final dimension of an aerogel is 1.0 cm x 1.0 cm x 0.18 cm.

Electrodeposition of MnO_2.

MnO_2 nanosheets were electrodeposited on the 3D printed graphene aerogel substrates in a two-electrode electrolytic cell using 0.1 M manganese acetate aqueous solution as the electrolyte and carbon paper as the counter electrode. Before electrodeposition, the graphene aerogel substrates were immersed in the electrolyte and degassed in a vacuum chamber until no bubble was formed. A pulse technique was used for electrodeposition, a repetitive cycle of which consists of an electrodeposition with constant current density of 10 mA cm^{-2} for 60 s followed by an open circuit (rest) period of 10 s. The electrolyte was also constantly stirred using a magnetic stir bar and a stir plate during the deposition process. The degas process, the pulse electrodeposition, and the constant stirring allow sufficient ion supply to all accessible substrate surfaces for homogeneous deposition. After electrodeposition, the 3D GA/MnO_2 composite material was washed with deionized water. An Ostwald ripening procedure was consequently conducted by hydrothermally treating the 3D GA/MnO_2 composite material in a 25 mL Teflon-lined stainless-steel autoclave filled with 20 mL deionized water at 90 ºC. The sample was then vacuum dried at room temperature overnight. The prepared samples are denoted as 3D GA/MnO_2-x, where x represents the number of pulse cycles (total minutes) of electrodeposition. The durations of the hydrothermal treatment for 3D GA/MnO_2-60, 3D GA/MnO_2-120, and 3D GA/MnO_2-180 are 40, 80 and 120 minutes, respectively. The MnO_2 mass loading of non-graded 3D GA/MnO_2-60, 3D GA/MnO_2-120, and 3D GA/MnO_2-180 was 24.0, 47.2 and 68.7 mg cm^{-2}, respectively. The MnO_2 mass loading of graded 3D GA/MnO_2-60, 3D GA/MnO_2-120, and 3D GA/MnO_2-180 was 22.7, 47.3 and 67.7 mg cm^{-2}, respectively.

Fabrication of Three-Electrode Cells.

The three-electrode cell for electrochemical tests of electrodes was fabricated in a 10 mL beaker cell with the working electrode held by a Pt electrode holder, a piece of carbon paper

as the counter electrode, a Pt wire as the pseudo-reference electrode, and 5 mL 1 M $LiClO_4$/acetonitrile solution as the electrolyte. The beaker cell was sealed to avoid the evaporation of acetonitrile during tests. All the electrolyte preparations, cell fabrications and electrochemical tests were conducted in a glovebox filled with dry Ar. The electrochemical tests were conducted using BioLogic EC-Lab SP-300 electrochemical workstation.

Electrodeposition of VO_x.

Mixed-valence vanadium oxide (VO_x) were electrodeposited on the graded 3D printed graphene aerogel substrates in a three-electrode electrolytic cell with 0.1 M of vanadium (IV) oxide sulfate hydrate + 0.2 M ammonium acetate aqueous solution mixture as the electrolyte, a piece of ring-shaped carbon cloth surrounding the working electrode as the counter electrode, and saturated calomel electrode (SCE) as the reference electrode. Before electrodeposition, the graphene aerogel substrates were immersed in the electrolyte and degassed in a vacuum chamber until no bubble was formed. A pulse cyclic voltammetry was used for electrodeposition, a repetitive cycle of which consists of a scanning from -1.5 to 1.5 back to -1.5 V vs. SCE at 20 mV s^{-1} followed by an open circuit (rest) period of 10 s. After 60 pulse cycles, the as-prepared vanadium oxide was further reduced under a constant potential of -1.5 V vs. SCE for 2 minutes in the same electrolyte to introduce lower-valence vanadium, yielding the graded 3D GA/VO_x composite electrode. The electrolyte was constantly stirred using a magnetic stir bar and a stir plate. After electrodeposition, the sample was washed with deionized water and vacuum dried at room temperature overnight. The VO_x mass loading was 36.0 mg cm^{-2}.

Fabrication of Lithium-Ion Hybrid Capacitor Devices.

The lithium-ion hybrid capacitor device was fabricated in a 10 mL beaker cell with the graded 3D GA/VO_x as a negative electrode, the graded 3D GA/MnO_2 as a positive electrode, and 5 mL 1 M $LiClO_4$/acetonitrile solution as the electrolyte. Both electrodes have a area of 0.2 cm^2 for charge balancing. Before assembling into the full device, both electrodes were

individually activated to charged state in a three-electrode cell using cyclic voltammetry by scanning at 5 mV s^{-1} for 3 cycles (0 to -2.6 V vs. Pt for VO_x, and -0.8 to 1.4 V vs. Pt for MnO_2). The beaker cell was sealed to avoid the evaporation of acetonitrile during tests. All the electrolyte preparations, cell fabrications and electrochemical tests were conducted in a glovebox filled with dry Ar. The electrochemical tests were conducted using BioLogic EC-Lab SP-300 electrochemical workstation.

Characterizations.

The SEM images of the samples were obtained by a field emission SEM (FEI Quanta 3D FEG dual beam) to investigate the surface morphologies. A powder X-ray diffractometer (Rigaku D-MAX 2200 VPC) was used to collect the XRD spectra of the samples. Diffraction spectra were recorded from a 2θ angle of 10-70°, with a step size of 0.01° at a rate of 0.1° min^{-1}. The elemental composition of the samples was analyzed by an XPS spectrometer (Thermo Scientific™ Nexsa G2) with Al Kα X-ray source. The frequency range of electrochemical impedance spectroscopy is 10^{-2} ~ 10^{6} Hz.

Micro-CT.

Tomography scans were performed on desktop laboratory micro-computed tomography scanner SkyScan 1272 (Bruker, Billerica, MA, USA) equipped with Hamamatsu L10101-67 (Hamamatsu Photonics, Shizuoka, Japan) X-ray source and XIMEA xiRAY16 (Ximea GmbH, Münster, Germany) detector. Camera sensor has a 4904 x 3280 resolution with 7.4 pixel size. All scans were done with source voltage and current tuned to 72 kV and 40 μA respectively. Camera-to-source and object-to-source distances were set to 274.8 mm and 55.7 mm respectively, resulting in projections with effective pixel size of 1.5 μm. A total of 900 projections were collected over a 180 degrees range.

Reconstructions were done using standard filter back projection algorithm of LTT (Livermore Tomography Tools, 1.6.38).[10] Reconstructed images were converted from 32-bits

to 8-bits by scaling intensity (add 2 then multiply by 40) and analyzed both in 2D and 3D using Fiji (ImageJ 1.53t)[11].

Trasatti Capacity Contribution Analysis

The gravimetric capacities ($Q_{G,CV}$) at different scan rates were first calculated from the corresponding cyclic voltammetry (CV) curves in Figure S13 (Supporting Information) using Equation 3.

$$Q_{G,CV} = \frac{S_{CV}}{2v} \tag{3}$$

where S_{CV} is the area enclosed by the CV curve (A V g^{-1}) and v is the scan rate (V s^{-1}). By assuming a semi-finite ion diffusion, a linear dependence of $Q_{G,CV}$ vs. $v^{-1/2}$ can be drawn at slow scan rates (1-5 mV s^{-1}). Due to the intrinsic electrical resistance of the electrode, the capacities calculated at high scan rates showed deviation from the linear trend, and thus were not included in the linear fitting. The y-intercept ($v \rightarrow +\infty$) of the extrapolated fitting line should represent the kinetically fast $Q_{surface}$ as capacities with relatively slow kinetic should be absent when $v \rightarrow +\infty$. Since $Q_{G,CV}$ at each scan rate is a sum of $Q_{surface}$ and Q_{bulk}, the percentage of capacity contribution from both $Q_{surface}$ and Q_{bulk} can therefore be calculated.

Calculations.

The gravimetric capacity (Q_G) and volumetric capacity (Q_V) of single electrodes were calculated based on the galvanostatic charging and discharging tests using Equation 4 and Equation 5, respectively.

$$Q_G = \frac{Q_{dis}}{m} \tag{4}$$

$$Q_V = \frac{Q_{dis}}{Ad} \tag{5}$$

where Q_G and Q_V are the gravimetric and volumetric capacities (mA h g^{-1} and mA h cm^{-3}, respectively), Q_{dis} is the discharging capacity (mA h) obtained from the galvanostatic discharging voltage profile of the single electrode, m is the mass loading of the active material

on the electrode (g), A is the geometric electrode working area (cm^2), and d is the thickness of the electrode (cm).

The gravimetric capacitance (C_G) and volumetric capacitance (C_V) of the lithium-ion hybrid capacitor device was calculated based on the galvanostatic charging and discharging tests using Equation 6 and Equation 7, respectively.

$$C_G = \frac{3600 \times Q_{dis}}{1000 \times \Delta U \times M} \quad (6)$$

$$C_V = \frac{3600 \times Q_{dis}}{1000 \times \Delta U \times V} \quad (7)$$

where C_G and C_V are the gravimetric and volumetric capacitances (F g^{-1} and F cm^{-3}, respectively), Q_{dis} is the discharging capacity (mA h) obtained from the galvanostatic discharging voltage profiles of the device, ΔU is the potential window (V) excluding the iR drop, M is the total mass loading of the active materials on both electrodes (g), and V is the total volume of both electrodes with active materials (cm^3).

The gravimetric capacity (Q_G) and volumetric capacity (Q_V) of the lithium-ion hybrid capacitor device was calculated based on the galvanostatic charging and discharging tests using Equation 8 and Equation 9, respectively.

$$Q_G = \frac{Q_{dis}}{M} \quad (8)$$

$$Q_V = \frac{Q_{dis}}{V} \quad (9)$$

where Q_G and Q_V are the gravimetric and volumetric capacities (mA h g^{-1} and mA h cm^{-3}, respectively), Q_{dis} is the discharging capacity (mA h) obtained from the galvanostatic discharging voltage profile of the device, M is the total mass loading of the active materials on both electrodes (g), and V is the total volume of both electrodes with active materials (cm^3).

The volumetric energy density (E_V, W h L^{-1}) and power density (P_V, W L^{-1}) of the lithium-ion hybrid capacitor device were calculated using the following equations:

$$E_{\mathrm{V}} = \frac{Q_{\mathrm{dis}} \times \Delta U}{2V} \tag{10}$$

$$P_{\mathrm{V}} = \frac{3600 \times E_{\mathrm{V}}}{t_{\mathrm{dis}}} \tag{11}$$

where Q_{dis} is the discharging capacity (mA h) obtained from the galvanostatic discharging voltage profiles of the device, ΔU is the potential window (V) excluding the *iR* drop, t_{dis} is the discharging time (s) in the galvanostatic discharging test, and V is the total volume of both electrodes with active materials (cm^3).

Supporting Information

Supporting Information is available from the Wiley Online Library or from the author.

Acknowledgements

The authors thank Dr. Tom Yuzvinsky from University of California, Santa Cruz for SEM images acquisition, and acknowledge the W. M. Keck Center for Nanoscale Optofluidics for use of the FEI Quanta 3D Dual-beam SEM. This work was performed under the auspices of the U.S. Department of Energy by Lawrence Livermore National Laboratory under contract DE-AC52-07NA27344. Lawrence Livermore National Security, LLC. The work was supported by the Laboratory Directed Research and Development (LDRD) program (20-ERD-019 and 23-SI-002).

Received: ((will be filled in by the editorial staff))

Revised: ((will be filled in by the editorial staff))

Published online: ((will be filled in by the editorial staff))

References

[1] a) X. Yang, C. Cheng, Y. Wang, L. Qiu, D. Li, *Science* **2013**, *341*, 534-537; b) D. Yu, K. Goh, H. Wang, L. Wei, W. Jiang, Q. Zhang, L. Dai, Y. Chen, *Nat. Nanotechnol.* **2014**, *9*, 555-562; c) Y. Xu, Z. Lin, X. Zhong, X. Huang, N. O. Weiss, Y. Huang, X. Duan, *Nat. Commun.* **2014**, *5*, 4554; d) G. Li, K. Mao, M. Liu, M. Yan, J. Zhao, Y. Zeng, L. Yang, Q. Wu, X. Wang, Z. Hu, *Adv. Mater.* **2020**, *32*, 2004632; e) J. Yan, Q. Wang, T. Wei, L. Jiang, M. Zhang, X. Jing, Z. Fan, *ACS Nano* **2014**, *8*, 4720-4729; f) J. B. Goodenough, A. Manthiram, *MRS Commun.* **2014**, *4*, 135-142; g) Y. Tao, X. Xie, W. Lv, D.-M. Tang, D. Kong, Z. Huang, H. Nishihara, T. Ishii, B. Li, D. Golberg, F. Kang, T. Kyotani, Q.-H. Yang, *Sci. Rep.* **2013**, *3*, 2975.

[2] A. Noori, M. F. El-Kady, M. S. Rahmanifar, R. B. Kaner, M. F. Mousavi, *Chem. Soc. Rev.* **2019**, *48*, 1272-1341.

[3] M. Yu, Y. Lu, H. Zheng, X. Lu, *Chem. Eur. J.* **2018**, *24*, 3639-3649.

[4] a) B. Yao, S. Chandrasekaran, J. Zhang, W. Xiao, F. Qian, C. Zhu, E. B. Duoss, C. M. Spadaccini, M. A. Worsley, Y. Li, *Joule* **2019**, *3*, 459-470; b) B. Yao, S. Chandrasekaran, H. Zhang, A. Ma, J. Kang, L. Zhang, X. Lu, F. Qian, C. Zhu, E. B. Duoss, C. M. Spadaccini, M. A. Worsley, Y. Li, *Adv. Mater.* **2020**, *32*, 1906652; c) Y. Song, T. Liu, B. Yao, M. Li, T. Kou, Z.-H. Huang, D.-Y. Feng, F. Wang, Y. Tong, X.-X. Liu, Y. Li, *ACS Energy Lett.* **2017**, *2*, 1752-1759; d) A. Huang, J. Chen, W. Zhou, A. Wang, M. Chen, Q. Tian, J. Xu, *J. Electroanal. Chem.* **2020**, *873*, 114392; e) W. Sun, F. Wang, S. Hou, C. Yang, X. Fan, Z. Ma, T. Gao, F. Han, R. Hu, M. Zhu, C. Wang, *J. Am. Chem. Soc.* **2017**, *139*, 9775-9778.

[5] a) C. Pan, R. Zhang, R. G. Nuzzo, A. A. Gewirth, *Adv. Energy Mater.* **2018**, *8*, 1800589; b) Y. Wang, Z. Hong, M. Wei, Y. Xia, *Adv. Funct. Mater.* **2012**, *22*, 5185-5193; c) D. Kundu, S. Hosseini Vajargah, L. Wan, B. Adams, D. Prendergast, L. F. Nazar, *Energy Environ. Sci.* **2018**, *11*, 881-892; d) G. Lee, D. Kim, D. Kim, S. Oh, J.

Yun, J. Kim, S.-S. Lee, J. S. Ha, *Energy Environ. Sci.* **2015**, *8*, 1764-1774; e) H.-Q. Wang, Z.-S. Li, Y.-G. Huang, Q.-Y. Li, X.-Y. Wang, *J. Mater. Chem.* **2010**, *20*, 3883-3889.

[6] a) K.-W. Nam, C.-W. Lee, X.-Q. Yang, B. W. Cho, W.-S. Yoon, K.-B. Kim, *J. Power Sources* **2009**, *188*, 323-331; b) L. Y. Chen, J. L. Kang, Y. Hou, P. Liu, T. Fujita, A. Hirata, M. W. Chen, *J. Mater. Chem. A* **2013**, *1*, 9202-9207; c) J. Duay, S. A. Sherrill, Z. Gui, E. Gillette, S. B. Lee, *ACS Nano* **2013**, *7*, 1200-1214.

[7] a) J. Zhao, Y. Zhang, H. Lu, Y. Wang, X. D. Liu, H. Maleki Kheimeh Sari, J. Peng, S. Chen, X. Li, Y. Zhang, X. Sun, B. Xu, *Nano Lett.* **2022**, *22*, 1198-1206; b) Y. He, W. Chen, X. Li, Z. Zhang, J. Fu, C. Zhao, E. Xie, *ACS Nano* **2013**, *7*, 174-182; c) L. Yu, W. Li, C. Wei, Q. Yang, Y. Shao, J. Sun, *Nano Micro Lett.* **2020**, *12*, 143; d) J. Zhao, Y. Zhang, X. Zhao, R. Wang, J. Xie, C. Yang, J. Wang, Q. Zhang, L. Li, C. Lu, Y. Yao, *Adv. Funct. Mater.* **2019**, *29*, 1900809; e) W. Kang, L. Zeng, S. Ling, C. Lv, J. Liu, R. Yuan, C. Zhang, *Adv. Funct. Mater.* **2021**, *31*, 2102184; f) T. Gao, Z. Zhou, J. Yu, J. Zhao, G. Wang, D. Cao, B. Ding, Y. Li, *Adv. Energy Mater.* **2019**, *9*, 1802578; g) C. Chen, Y. Zhang, Y. Li, J. Dai, J. Song, Y. Yao, Y. Gong, I. Kierzewski, J. Xie, L. Hu, *Energy Environ. Sci.* **2017**, *10*, 538-545; h) J. Yang, L. Lian, H. Ruan, F. Xie, M. Wei, *Electrochim. Acta* **2014**, *136*, 189-194; i) T. Zhai, F. Wang, M. Yu, S. Xie, C. Liang, C. Li, F. Xiao, R. Tang, Q. Wu, X. Lu, Y. Tong, *Nanoscale* **2013**, *5*, 6790-6796; j) P. Chang, H. Mei, Y. Tan, Y. Zhao, W. Huang, L. Cheng, *J. Mater. Chem. A* **2020**, *8*, 13646-13658.

[8] a) S. Ardizzone, G. Fregonara, S. Trasatti, *Electrochim. Acta* **1990**, *35*, 263-267; b) D. Baronetto, N. Krstajić, S. Trasatti, *Electrochim. Acta* **1994**, *39*, 2359-2362.

[9] C. Zhu, T. Liu, F. Qian, T. Y.-J. Han, E. B. Duoss, J. D. Kuntz, C. M. Spadaccini, M. A. Worsley, Y. Li, *Nano Lett.* **2016**, *16*, 3448-3456.

[10] K. M. Champley, T. M. Willey, H. Kim, K. Bond, S. M. Glenn, J. A. Smith, J. S. Kallman, W. D. Brown, I. M. Seetho, L. Keene, S. G. Azevedo, L. D. McMichael, G. Overturf, H. E. Martz, *NDT & E Int.* **2022**, *126*, 102595.

[11] J. Schindelin, I. Arganda-Carreras, E. Frise, V. Kaynig, M. Longair, T. Pietzsch, S. Preibisch, C. Rueden, S. Saalfeld, B. Schmid, J.-Y. Tinevez, D. J. White, V. Hartenstein, K. Eliceiri, P. Tomancak, A. Cardona, *Nat. Methods* **2012**, *9*, 676-682.